



Pure and Antimony-doped Tin Oxide Nanoparticles for Fluorescence Sensing and Dye Degradation Applications

Deepika Garg¹ · Gurdeep Singh¹ · Heena Rekhi³ · Manpreet Kaur¹ · Rajpal Verma¹ · Karamjit Singh² · Ashok Kumar Malik¹

Received: 31 March 2023 / Accepted: 21 May 2023 / Published online: 9 June 2023
© The Author(s), under exclusive licence to Springer Science+Business Media, LLC, part of Springer Nature 2023

Abstract

Luminescent antimony doped tin oxide nanoparticles have drawn tremendous attention from researchers due to its low cost, chemical inertness and stability. Herein, a quick, facile and economic hydrothermal/solvothermal method was utilized for the preparation of antimony doped (1%, 3%, 5%, 7% and 10%) tin oxide nanoparticles. The antimony doping in a reasonable range can change the properties of SnO₂. As such, a lattice distortion increases with increase in doping, which is evidenced through crystallographic studies. It was found that the highest photocatalytic degradation efficiency of malachite green (MG) dye of about 80.86% was achieved with 10% Sb-doped SnO₂ in aqueous media due to small particle size. Moreover, 10% Sb-doped SnO₂ also showed the highest fluorescence quenching efficiency of about 27% for Cd²⁺ of concentration 0.11 µg/ml in the drinking water. The limit of detection (LOD) comes out as 0.0152 µg/ml. This sample selectively detected the cadmium ion even in the presence of other heavy metal ions. Notably, 10% Sb-doped SnO₂ could appeared as a promising sensor for fast analysis of Cd²⁺ ions in real samples.

Keywords Tin oxide · Sb-doping · Morphology · Crystallography · Heavy metal ions · Sensing, photocatalysis · Cadmium ions

Introduction

With the growth of modern society, different pollutants (e.g., nitroaromatic compounds (NACs), toxic gases, metal ions) discharged into an environment. Metals ions are widely distributed in different geographical regions [1]. Certain metal ions are essential for growth of human beings, while others can cause serious problems even at trace concentration. Cadmium is highly toxic causing serious health problems such as cancer, bone degeneration, and kidney disorder. An International agency for Research and Cancer (IARC) stated that Cd at high concentration is carcinogenic and can cause chronic renal failure [2, 3]. Even at low concentration, Cd can cause causing damage of kidney, fragile bone, and lung

damage. So, there is need to develop a selective and sensitive method for the detection of cadmium.

Various technologies like gas chromatography-mass spectrometry (GC-MS), liquid chromatography-mass spectrometry (LC-MS), energy dispersive X-ray spectroscopy (EDX), surface enhanced raman spectroscopy (SERS), high-performance liquid chromatography (HPLC), electron capture detection (ECD), proton transfer reaction mass spectrometry (PTR-MS), nuclear quadrupole resonance (NQR), neutron activation analysis (NAA) and ion mobility spectrometry have been used for the detection of cadmium [4–6], however these are highly expensive and require highly sophisticated instruments [5]. Hence, these techniques cannot be utilized for on-site field testing. Instead, fluorescence-quenching-based chemical detection proved to be simple, sensitive, rapid and less expensive method for the quick detection of cadmium ions [4]. Due to economic and selective detection by fluorescent material it has become the major concern to be utilized on large scale.

Besides metal ions, hazardous dyes discharged from various textile industries into water can cause serious water pollution. Dyes have serious environmental and human health issues due to their carcinogenic and toxic effects [7, 8]. So,

✉ Ashok Kumar Malik
malik_chem2002@yahoo.co.uk

¹ Department of Chemistry, Punjabi University,
Patiala 147 002, Punjab, India

² Department of Physics, Punjabi University, Patiala 147 002,
Punjab, India

³ GSSDGS Khalsa College, Patiala 147 001, Punjab, India

as a remedy of dye effluents various methods have been utilized like adsorption on high surface area support, sedimentation, chemical coprecipitation, ion exchange method and biological membranes [9]. But, these methods are not preferred to large extent due to their expensive equipment's, time consumption and conversion of main pollutant into secondary pollutant, which can be even more hazardous. In addition to these methods, some biochemical and physiochemical methods can be utilized for decolourization of dyes from the textile industries due to their inflexibility towards chemical oxidation and photocatalytic stability. However, recently researchers have set their focus on the utilization of semiconductor metal oxide for degradation of dyes.

To resolve the afore discussed issues, there is need to develop such materials, which can act both as photocatalyst and as sensor. Semiconductor is one of the potential candidates which act as sensor and photocatalyst. Among various available semiconductors, SnO_2 , ZnO , Fe_2O_3 and CeO_2 are the most frequently used semiconductor due to their photochemical stability, low cost, non-toxicity and simple preparation [9]. Among these, SnO_2 can be utilized for the purpose of photocatalytic degradation of dyes and sensing of heavy metal ions, effectively. According to Bouras et al. (2014), the SnO_2 material has good chemical and thermal stability. SnO_2 is widely utilized as a semiconductor material owing to its remarkable physical and chemical properties. Further, SnO_2 is an n-type semiconductor which is widely utilized in different areas like transparent electrodes, photocatalysts, batteries, transistors, fluorescence sensors, gas sensors, and other devices [10]. Notably, the bandgap and chemical stability of SnO_2 is equivalent to that of a popular photocatalyst, titanium dioxide (TiO_2). Therefore, SnO_2 was chosen as a superior photocatalyst in the current examination. Additionally, SnO_2 has no negative health consequences whether inhaled or injected because it is poorly absorbed by the human body. A green technology, photocatalytic oxidation of organic contaminants in the presence of semiconductors like tin oxide (SnO_2) appears to be a very promising method for treating water. The first obstacle limiting the widespread technological application of SnO_2 is its large band gap (3.6 eV) [11], which needs UV irradiation for photocatalytic activation. However, the solar radiation mainly constitutes from the UV, visible, and infrared radiations with percentage of 5–7%, 46%, and 47%, respectively. As, UV light only makes up a small portion of the sun energy (5%) compared to visible light (45%) so it can't provide the sufficient energy for the photocatalytic activity of SnO_2 [12]. Therefore, large SnO_2 band gap and non-availability of UV radiations through sun light will limit its effectiveness. To achieve the great photocatalytic efficiency, the band gap of SnO_2 must be shifted in such a way that it shows the optical absorbance in the visible light. Such modulation in band gap can be achieved through the doping. At the end, it should be

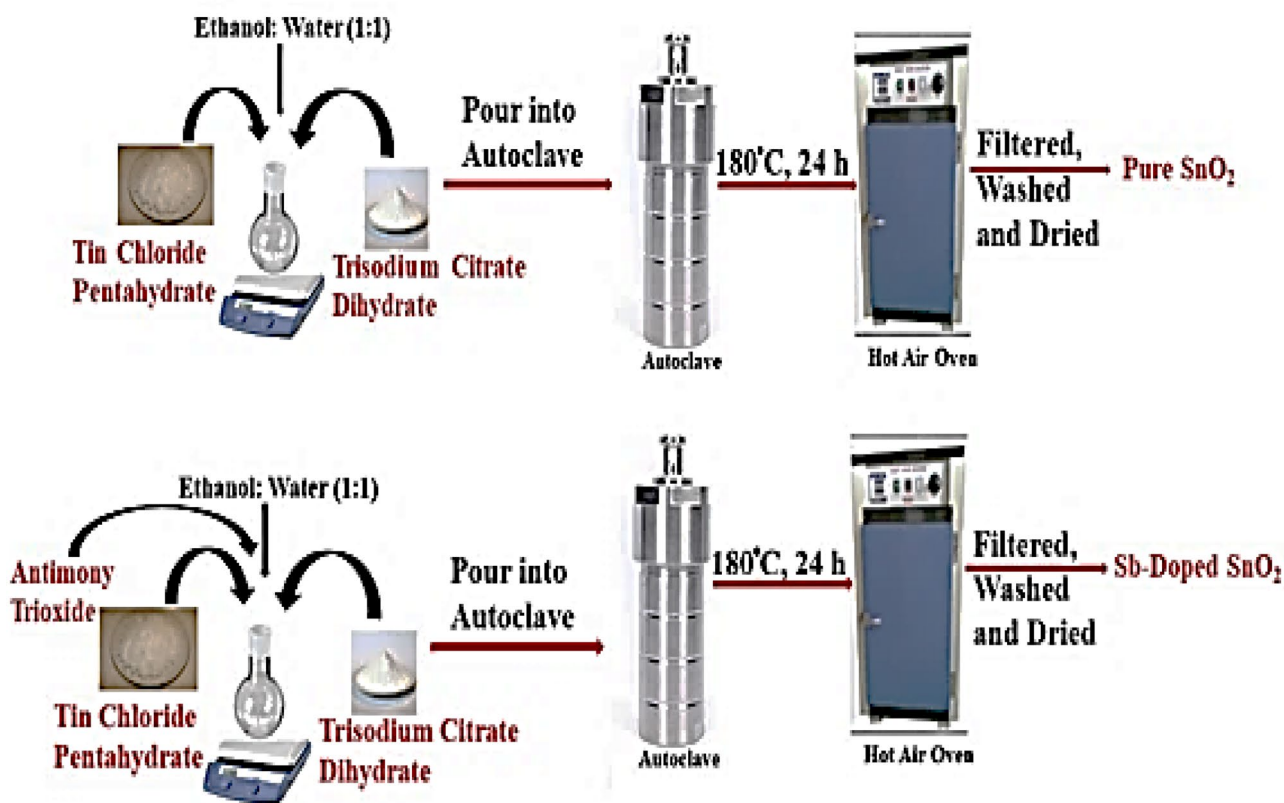
mentioned here that the shift in SnO_2 optical response from the UV to the visible spectral range will have a profoundly positive impact on the photocatalytic activity of the studied material. For the purpose of shifting optical absorbance in the visible region of solar spectrum various attempts have been utilized like coupling of SnO_2 with gold [13], but this method proved to be unsuccessful for this purpose. Hence, a number of researchers have moved towards the doping of semiconductor metal oxide material with particular metal for shifting optical absorbance. A variety of dopants can be utilized for the modification of band gap resulting in large change in physical and chemical properties. In literature various reports have been demonstrated in which band gap has been tuned by introducing particular dopants with particular yield. As an example, tungsten doped tin oxide [14, 15], indium doped tin oxide [16], fluorine doped tin oxide [17, 18], antimony doped tin oxide [19–22] and zinc doped tin oxide [23, 24] have band gap tuned to 4.05–4.22 eV, 3.62–4.03 eV, 3.7–3.8 eV, 3.1–3.9 eV and 3.58–3.97 eV, respectively. With doping optical properties get changed by amplifying band gap and luminescent centres in the visible region. Most common dopant used for SnO_2 is antimony (Sb). In this trivalent Sb^{3+} ions can easily replace tetravalent Sn^{4+} leading to the shifting the fermi level towards the conduction band (CB) [25]. The mechanism of photocatalytic degradation is based on excitation of SnO_2 resulting in formation of electron-hole pair production, which further produce highly reactive OH^\bullet and $\text{O}_2^{\bullet-}$ for the degradation of organic and inorganic pollutants [26, 27]. However, proper reactor design and optimized conditions are necessary for efficient photocatalytic activity.

To the best of our knowledge, Sb-doped SnO_2 nanostructures have not been explored to act as photocatalyst for dye degradation and luminescent sensor for detection of heavy metal ions through sensing. So, here our main focus is to investigate and present the effect of doping on the morphological, optical, photocatalytic and sensing applications. For the investigation of photocatalytic activity Sb-doped SnO_2 have been utilized using malachite green (MG) as a test contaminant in the aqueous media. Additionally, Sb-doped SnO_2 can be effectively used for selective detection of Cd^{2+} with the lowest concentration upto 10 ppb even in the presence of other heavy metal ions.

Experimental Section

Materials

All the chemical reagents and solvents are of analytical grade and can be utilized without further purification. Tin(IV) chloride pentahydrate ($\text{SnCl}_4 \cdot 5\text{H}_2\text{O}$), trisodium citrate dihydrate ($\text{C}_6\text{H}_5\text{Na}_3\text{O}_7 \cdot 2\text{H}_2\text{O}$), antimony trioxide



Scheme 1 Schematic diagram showing synthesis of undoped and Sb-doped SnO₂

(Sb₂O₃), cadmium sulphate (CdSO₄) and ethanol (C₂H₅OH) were purchased from Sigma-Aldrich, India. Malachite Green (MG) dye was purchased from Merck Pvt. Ltd. India.

Synthesis of Sb-doped SnO₂ Nanostructures

Tin chloride pentahydrate (SnCl₄·5H₂O, 8mmol (0.90256 g)) and trisodium citrate dihydrate (C₆H₅Na₃O₇·2H₂O, 8 mmol (2.064 g)) were dissolved in 30 ml of ethanol:water (1:1). The resulting solution was magnetically stirred for 1 h followed by pouring in a Teflon-lined stainless steel autoclave. The autoclave was properly sealed, heated in vacuum oven by maintaining temperature to be 180 °C for 24 h and cooled to room temperature. Afterwards, the obtained precipitates were collected from the autoclave and rinsed with ethanol & distilled water mixture several times for the removal of impurities. Later, these precipitates were annealed at 600 °C for 2 h. Similar procedure was adopted for the synthesis of Sb-doped SnO₂ nanostructures, with the only variation of addition of antimony trioxide (Sb₂O₃) to tin (IV) chloride pentahydrate solution before the addition of trisodium citrate dihydrate (C₆H₅Na₃O₇·2H₂O). The concentration of Sb was varied from (1–10) mol%. Finally, Sb-doped SnO₂ samples

were collected. This whole procedure of synthesis is shown through a Scheme 1.

Characterizations

Various analytical techniques were opted for the investigation of synthesized sample via its crystallographic, morphological, compositional and optical analysis. For the record of crystallographic parameters of the prepared samples, Powder X-ray Diffractometer XPERT PRO [CuK_α X-ray (λ = 1.5406Å), 1800 W (45 kV, 40 mA)] in 2θ range 10° to 60° keeping step size of 0.013° at scan speed of 0.001° sec⁻¹ was used. The morphological investigations were performed on JEOL, JEM 2100 PLUS high resolution transmission electron microscope (HRTEM) and JEOL, JSM-6510LV scanning electron microscope (SEM). Energy dispersive spectroscopy (EDS) attached with SEM, was used for the chemical and elemental composition of the prepared samples, respectively. JEOL JEM-2100 plus high-resolution transmission electron microscope (HRTEM) is used to characterize the morphology of the sample. For the functional group analysis, Fourier Transform Infrared Spectroscopy (FTIR, PerkinElmer spectrometer) was recorded in the range 4000–400 cm⁻¹. UV-Visible

spectrophotometer (Shimadzu UV-Vis 1600) was used for absorption/degradation studies, while Shimadzu RF-5301PC spectrofluorometer was opted for photoluminescence studies.

Photocatalytic Experiment

At room temperature, the photocatalytic degradation of malachite green (MG) experiments were performed using pure and Sb-doped SnO₂ as a nano-photocatalyst under UV irradiation exposure. UV-Visible illumination was provided by an assembly of 4 UV tubes of 18 W each as a light source. To carry out this experiment, firstly a stock solution (1 L) of dye was prepared by dissolving 3 mg of MG dye in aqueous media. Then 20 mg of nano-photocatalyst (each) was added into 100 ml of MG solution followed by stirring in dark for 1 h to reach adsorption-desorption equilibrium. After this the equilibrated solution was exposed to UV irradiation for 60 min. Samples of 3–5 ml (each) were collected after every 10 min of UV exposure from photocatalytic chamber. These were analysed using UV-Visible absorption spectrophotometer to calculate the remnant dye concentration via monitoring the absorption maxima peak ($\lambda_{\text{max}} = 617 \text{ nm}$).

Concentration Dependent Luminescence Quenching Behaviour of Sb-doped SnO₂ Nanostructure Via Adding Different Concentration of Cd²⁺ Ion

Stock solution of SnO₂ and Sb-doped SnO₂ (1 mol%, 3 mol%, 5 mol%, 7 mol% and 10 mol%) were prepared by dissolving 10 mg of respective component in 10 ml of DMF. The stock solution of cadmium was prepared by dissolving 10 mg of cadmium sulphate (CdSO₄) in 10 ml of DMF solvent (1000ppb). Various concentrations of Cd²⁺ (5 ppb, 10 ppb, 15 ppb, 20 ppb, 25 ppb) were prepared from stock solution with careful quantitative dilution. The fluorescence detection of Cd²⁺ was done using Sb-doped SnO₂ NPs suspension in DMF at room temperature. For the purpose of proper analysis, 100 μl portion of Sb-doped NPs solution was added in 1 ml of different concentrations of Cd²⁺ (0–25 ppb) with addition of 1.9 ml of dilution with continuous stirring and allowed to stand at room temperature for 15 min. The photoluminescence intensity of the resulting solution was recorded on spectrofluorometer at excitation wavelength 340 nm ($\lambda_{\text{ex}} = 340 \text{ nm}$).

Result and Discussion

X-ray Diffraction Analysis

Figure 1 exhibits an experimental powder X-ray diffraction pattern for the synthesized samples. Tetragonal Rutile structure of SnO₂ have been evaluated through the well indexing of all the diffraction peaks [JCPDS no. 41-1445,

$a = b = 0.4738 \text{ nm}$ and $c = 0.3187 \text{ nm}$, space group P42/nm (136)]. The peaks appeared at 26.74°, 32.87°, 36.11° and 58.70° can be indexed to the lattice planes of (110), (101), (200) and (002), respectively [28–30]. Pure and single phase Sb-doped SnO₂ sample formation has been confirmed without any impurity due to absence of extra diffraction peak. The comparison with the previous studies shows the formation of desired nanoparticles [31, 32]. Table 1 represent calculated crystallographic parameters of the sample through XRD data and Debye's Scherrer formula. The decrease in the values of lattice constant ($a = b$, c) as well as crystallite size (D) with increase in the Sb doping concentration proved the suppress in the growth of larger SnO₂ crystallites [33]. The shrinkage or expand in the lattice can be explained through Vegard's Law, according to which the substitutional incorporation of the dopant ions in the host lattice leads to shrinkage, while dopant incorporation in the interstitial sites between Sn and O leads to expansion [34, 35]. From

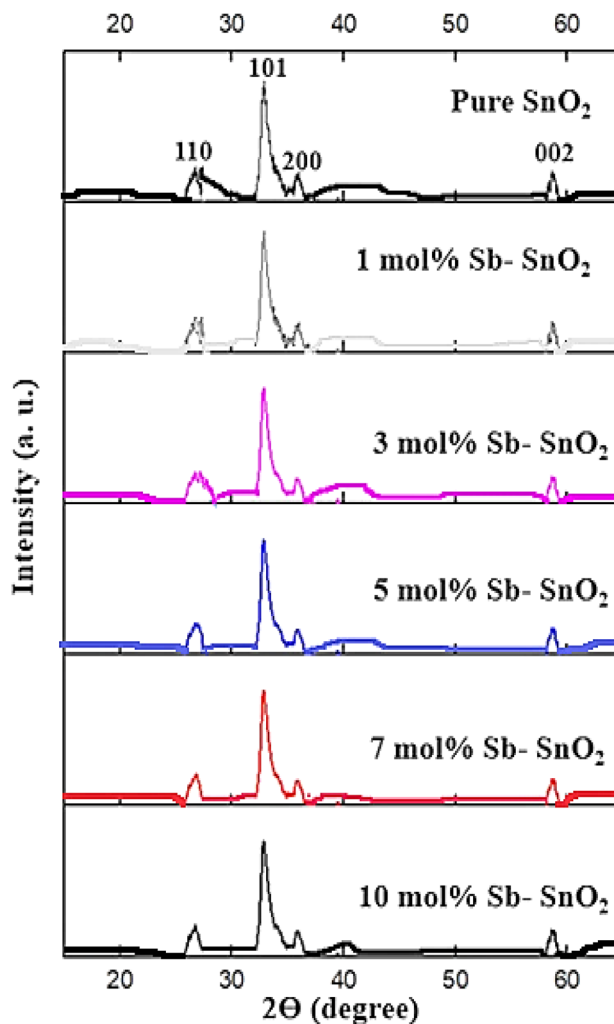


Fig. 1 XRD diffractogram of undoped and Sb-doped (1–10 mol%) SnO₂

Table 1 Crystallographic parameters of pure and Sb-doped SnO₂ from XRD patterns

Specimen	Lattice parameter a = b (Å)	Lattice parameter c (Å)	Crystallite size D (nm)
Pure SnO ₂	4.7636	3.1949	33.58
1 mol% Sb-SnO ₂	4.7564	3.1929	33.46
3 mol% Sb-SnO ₂	4.7330	3.1834	32.15
5 mol% Sb-SnO ₂	4.7318	3.1823	29.16
7 mol% Sb-SnO ₂	4.7225	3.1821	28.21
10 mol% Sb-SnO ₂	4.7211	3.1815	26.63
Std. JCPDS 41- 1445	4.7382	3.1871	-----

the results of Table 1, it can be predicted that there is substitutional doping of antimony ions into SnO₂ host lattice.

FT-IR Analysis

The Fourier Transform Infrared Spectroscopy (FT-IR) is used for the estimation of functional groups, detail of chemical bonding in existed elements and presence of impurities even in low levels. Figure 2 shows the FT-IR spectra of SnO₂ as well as Sb (1,3,5,7,10 mol%) doped SnO₂ in the transmission mode. For pure sample the characteristic peak at 637 cm⁻¹ is assigned to O-Sn-O stretching vibration mode and the band in the 2500–3500 cm⁻¹ along the O-H stretching. The peak at 1628 cm⁻¹ corresponds to C=C stretching. Role of Sb in SnO₂ by FTIR confirmed by Zhang et al.

Fig. 2 FTIR spectra of **a** pure; **b** 1 mol%; **c** 3 mol%; **d** 5 mol%; **e** 7 mol% and **f** 10 mol% Sb-doped SnO₂ samples

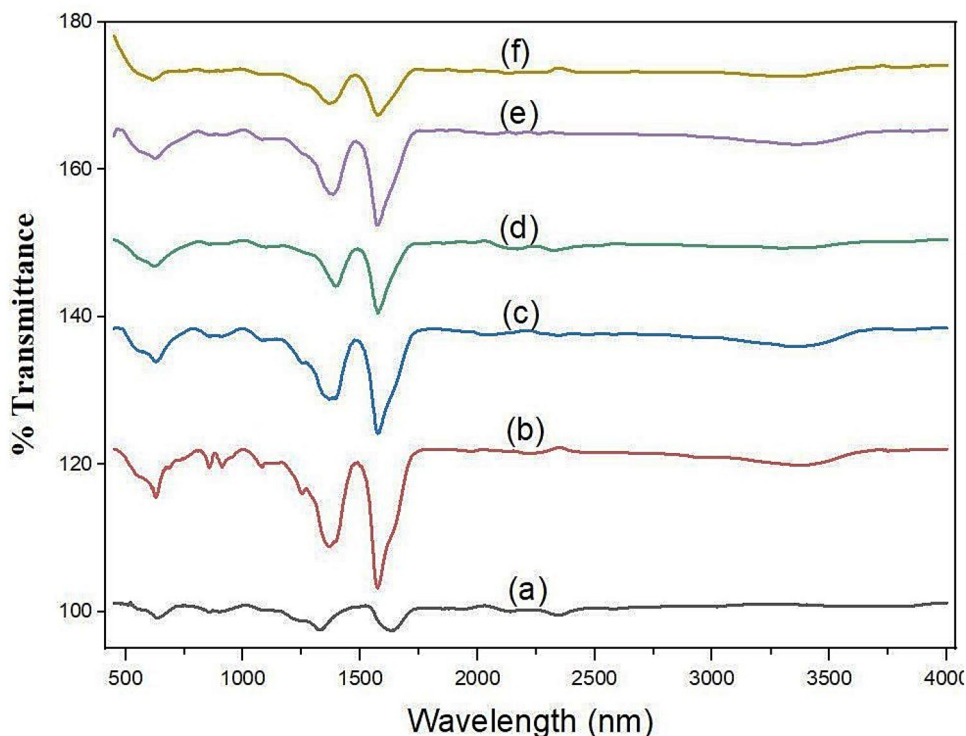


Figure 2, shows a small shift from 637 cm⁻¹ with increase in Sb doping concentration, which confirms the substitution in the SnO₂ by Sb, explained by Hooke's law. It is clear that the bonds formed by heavy atoms vibrate at lower frequencies and with lower mass vibrate at higher vibrational frequency. As the atoms of Sb are heavier than Sn ones (121.7 vs. 118.7 g/mol), resulting in shifting of Sn-O absorption band towards lower wave number after substitution of Sn by Sb. So, FTIR studies clearly confirms that Sb has taken place of Sn atoms after doping in SnO₂ nanostructure.

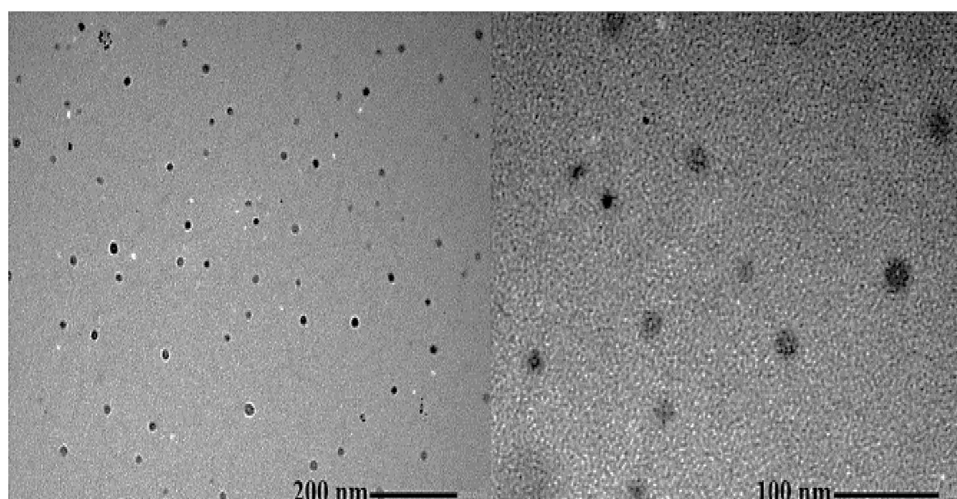
HR-TEM Analysis

Crystal structure and difference in microstructure have been further studied by High Resolution Transmission Electron Microscopy (HR-TEM). Figure 3 represents TEM micrograph, which depicts porous and hollow structure of pure SnO₂ nanoparticles. The images show grains like morphology with 10–15 nm size.

Morphological and Compositional Analysis

EDS spectra of Sb-doped SnO₂ samples have been recorded for the investigation of elemental composition as shown in Fig. 4a, b. The presence of Sb, Sn and O in the synthesized sample can be confirmed by presence of peaks of tin (Sn), oxygen (O) and antimony (Sb) in the spectra. Detailed analysis of the EDS spectrum of undoped SnO₂ samples reveals that tin (Sn) and oxygen (O) have weight% (atomic %)

Fig. 3 h-TEM micrograph of synthesized pure sample of SnO_2



values 58.66% (13.56%) and 41.34% (86.44%), respectively. Whereas, analysis of EDS spectrum of 10% Sb-doped SnO_2 shows sample comprises of tin (Sn), oxygen (O) and antimony (S) have weight% (atomic%) values 40.80% (9.31%), 49.36% (87.56%) and 9.84% (3.13%), respectively. The morphological features of as-prepared samples were investigated by SEM, as shown in Fig. 5a-f. As confirmed by SEM images, pure SnO_2 comprises irregular nanosheet like morphology, grown in very high density. The morphology of 1% Sb-doped SnO_2 is shown in Fig. 5b. Compared with the undoped sample, the products are composed of SnO_2 flakes like morphology, in place of nanosheet. 3% Sb-doped SnO_2 nanostructures, as shown in Fig. 5c consist of dense flakes of longer length of SnO_2 . Mix morphology of small SnO_2 nanorods has been observed in the case of 5% Sb-doped

SnO_2 (Fig. 5d). By, increasing the Sb dopant concentration from 5 to 7%, the morphology comprises only SnO_2 mixture of small spheres and nanorods, in place of nanorods along with spheres (as observed in 3% Sb doped SnO_2), as seen in Fig. 5e. Maximum dopant concentration of Sb (10 mol%) in SnO_2 host lattice results in SnO_2 increase in the number of spheres and increase in the length of nanorods (Fig. 5f) as compared to nanorods observed in the case of (Sb: SnO_2 7%). Interestingly, from SEM images, it has been observed that the morphology of SnO_2 nanosheets changes first into flakes, then from flakes to dense flakes and finally results into nanorods of longer length along with small spheres, after the doping of Sb element into pure SnO_2 . The basic reason behind this is the substitutional incorporation of Sb ions into SnO_2 host lattice, which modifies the local

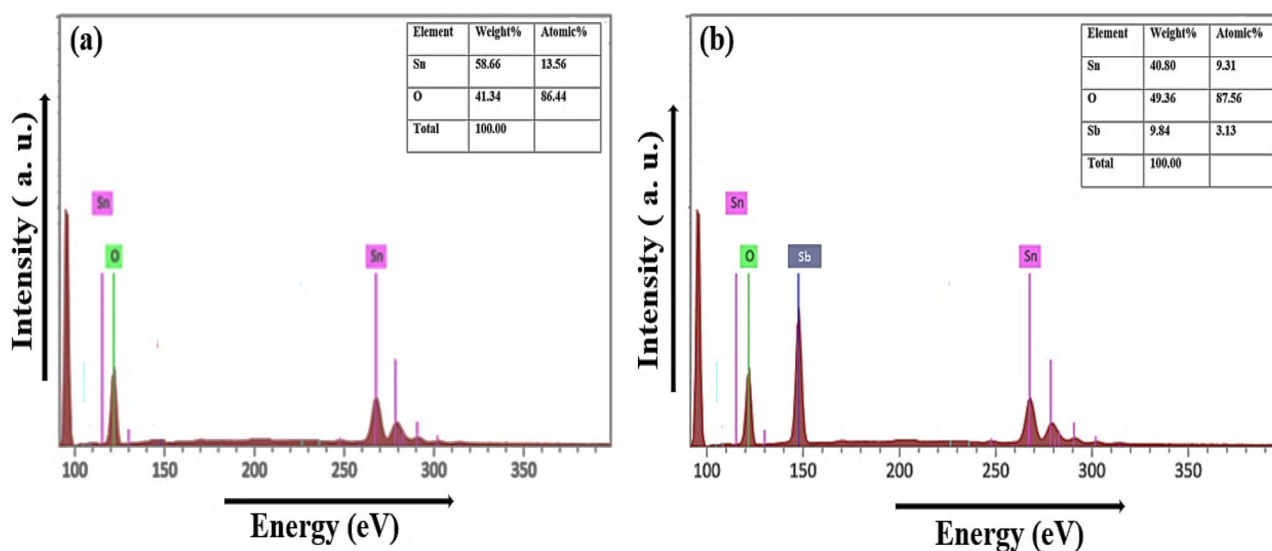


Fig. 4 EDS spectra of **a** pure SnO_2 ; **b** 10 mol% of Sb-doped SnO_2

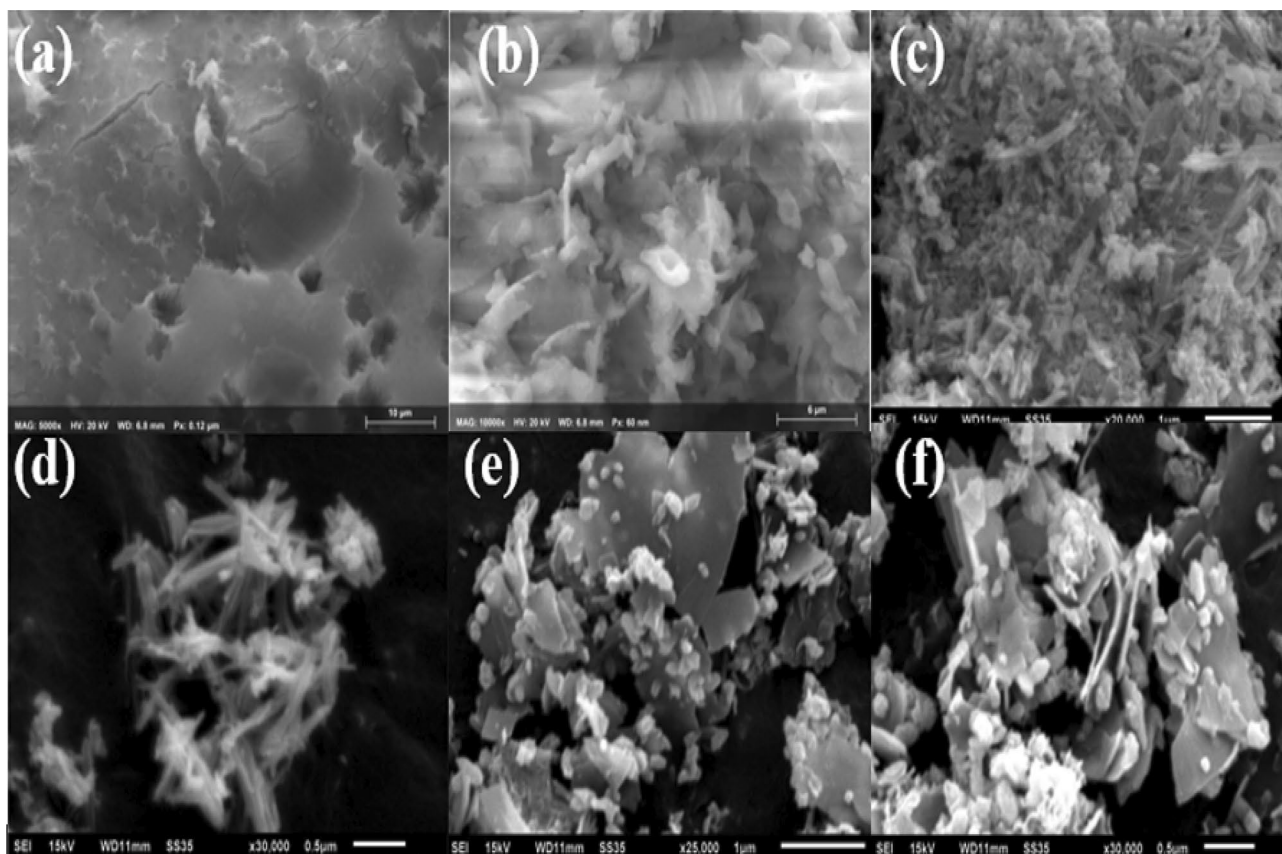


Fig. 5 SEM image of **a** Pure SnO_2 ; **b** 1 mol %; **c** 3 mol %; **d** 5 mol %; **e** 7 mol % and **f** 10 mol % antimony doped SnO_2 nanostructures

structure of host lattice, thereby leading to the variation in the surface energy of some crystal planes, which further changes their growth rate. Therefore, antimony serves as a structure-modifying agent in the growth of nanorods. It can be observed from Fig. 5a–f that the diameter and thickness of various morphologies of nanostructures is reduced gradually with the increase in the amount of Sb doping, which is the result of suppression of grain boundary migration and increasing the energy barrier for grain growth.

Optical Analysis

Optical properties have been investigated via UV-Vis absorption spectra of undoped SnO_2 and Sb-doped SnO_2 (1,3,5,7,10 mol %) recorded in the wavelength range of 250 to 650 nm. Figure 6a represents the plot of absorbance versus wavelength as an absorption spectra recorded at room temperature for all samples. Here, the presence of impurity centres can greatly influence the absorbance of light by nanoparticles. Due to photo-excitation of electrons from valence band to conduction band, all the doped samples

show absorbance around 280–320 nm. For the detailed analysis of presence of defects in a synthesized pure and doped sample, PL emission spectra has been recorded by providing excitation wavelength at 350 nm as shown in Fig. 6b. From 0 to 7 mol% Sb dopant concentration, the intensity of strong bands at 419 nm gradually increases, however at higher doping concentrations, such 10 mol%, a steady decrease in intensity has been observed. Sb^{3+} ions can easily take the role of Sn^{4+} ions at lower concentrations (1 to 7 mol%). However, in order to compensate for the -1 charge of the substituted Sn site, oxygen vacancies must also be created somewhere in the lattice, which raises the defect levels and improves the material visible emission in the fluorescence spectra. At higher Sb dopant concentrations (10 mol%), the excited electrons may transition from the valence band to new energy levels that have been created by the dopant near to the conduction band. Notably, the rate of recombination of photogenerated charge carriers decreases and photocatalytic activity increases when the excited electrons and excited holes are retained by oxygen vacancies and dopant Sb ions, respectively.

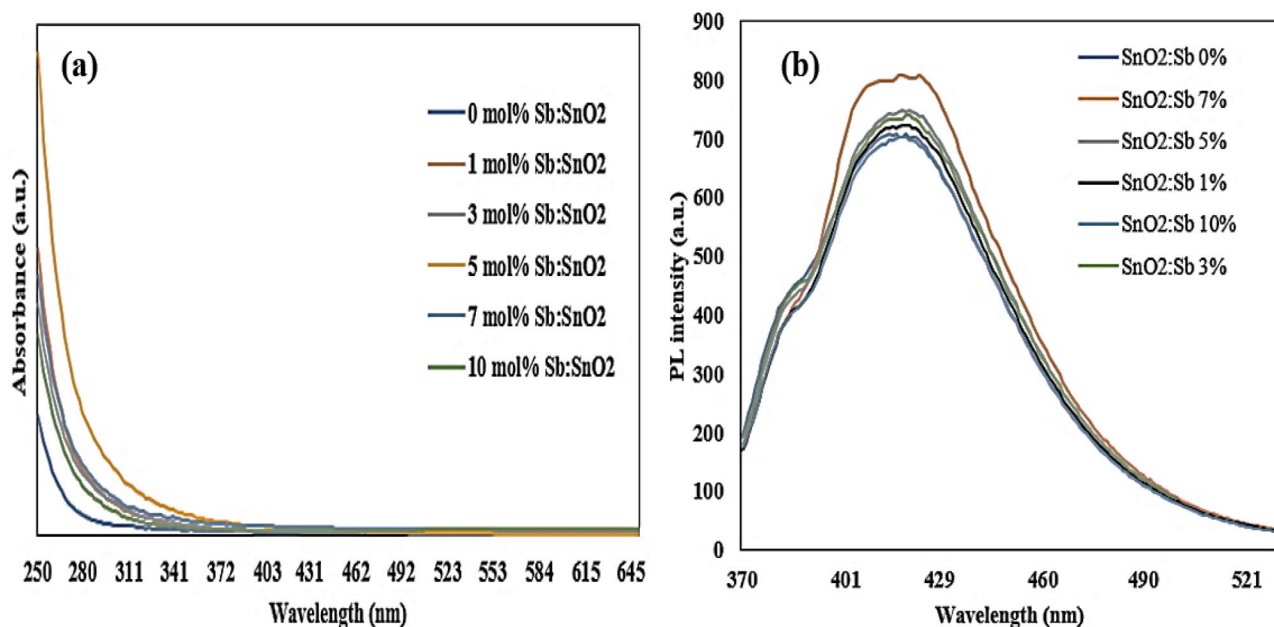


Fig. 6 **a** UV-Vis absorption spectra of pure SnO₂ and Sb-doped SnO₂ (1 mol%, 3 mol%, 5 mol%, 7 mol% and 10 mol%), **b** PL emission spectra of SnO₂ and Sb-doped SnO₂ (Sb: 1%, 3%, 5%, 7% and 10%)

Photocatalytic Degradation of Malachite Green Dye by Undoped and Sb-doped SnO₂ Samples

To investigate photocatalytic activity of undoped and Sb doped (1%, 3%, 5%, 7% and 10%) SnO₂ samples towards organic pollutants, malachite green (MG) was selected as a

test contaminant in aqueous medium under UV exposure. As shown in recorded spectra (Fig. 7a-f) the absorption peak situated at 617 nm shows highest absorbance, which was utilized for observing the remnant dye concentration for different duration of UV exposure in the presence of photocatalyst [undoped and Sb-doped SnO₂]. To examine

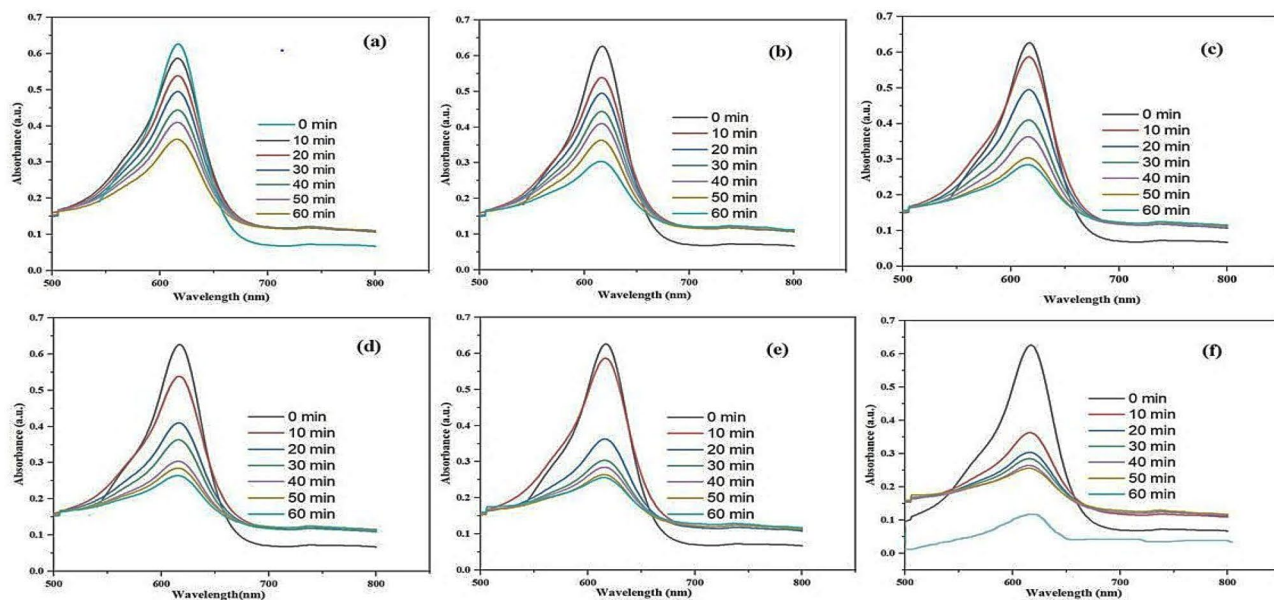
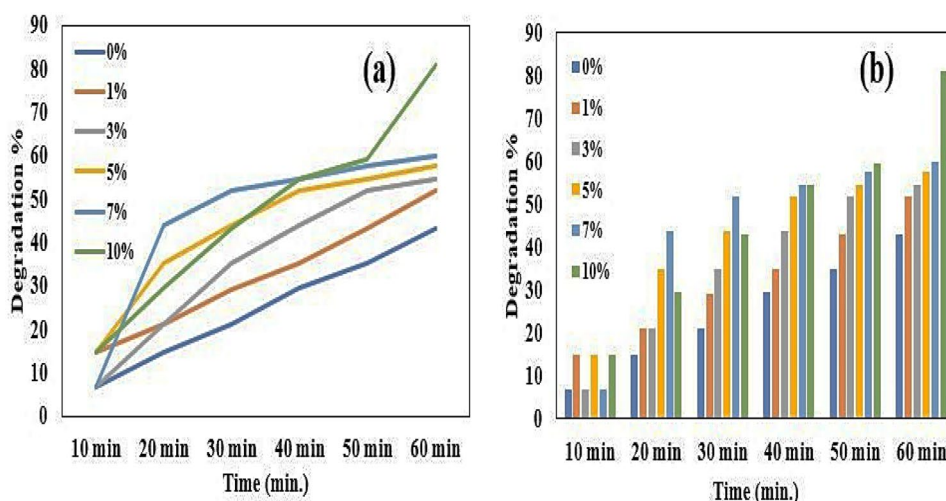


Fig. 7 Absorption spectra of malachite green dye degradation as a function of time in presence of **a** pure SnO₂; **b** 1% Sb doped SnO₂; **c** 3% Sb doped SnO₂; **d** 5% Sb doped SnO₂; **e** 7% Sb doped SnO₂; **f** 10% Sb doped SnO₂

Fig. 8 **a** Plot showing variation in degradation of dye percentage as a function of time for undoped and different Sb% doped SnO₂ samples; **b** Quantitative variation in degradation % as a function of time



photocatalytic performance of undoped and Sb-doped SnO₂ time dependent absorption spectra of dye solution was recorded with time gap of 10 min of UV light exposure. Here, we can see a clear decrease in intensity of absorption maxima ($\lambda_{\max} = 617$ nm) of dye solution for undoped and Sb-doped samples with the passage of time under UV exposure. For further detailed investigation of degradation percentage for aqueous solution of malachite green (MG) dye by undoped and Sb-doped SnO₂ samples, a plot of degradation percentage by different samples as a function of UV exposure time was drawn as shown in Fig. 8a. Additionally, for quantitative investigation of degradation percentage a plot in form of histogram was drawn (Fig. 8b), which shows increase in degradation percentage with increase in UV exposure and maximum degradation efficiency was shown by 10% Sb-doped SnO₂, which is 80.86% with in 60 min of UV exposure followed by 59.8%, 57.73%, 54.70%, 51.83% and 43.06% for 7%, 5%, 3%, 1% and 0% Sb-doped SnO₂, respectively. Here, it was depicted that degradation percentage increase with both increase in UV exposure time as well as doping percentage of Sb. The main reason behind the excellent degradation percentage of 10% Sb-doped SnO₂ was its specific morphology of flakes, this may result in formation of large no of active sites for the adsorption of reactant species and oxygen molecules resulting in their effective transport. For the calculation of degradation percentage by photocatalyst the following equation can be utilized:

$$\text{Degradation \%} = \frac{A_0 - A}{A_0} \times 100$$

where, A_0 and A represents absorbance of dye solution at 0 min and particular time interval of UV exposure, respectively. Figure 9 represents the schematic mechanism of degradation of dye by photocatalyst (SnO₂). Basically, degradation of dye molecules depends on amount of hydroxyl radical (OH[•]). So, photocatalytic efficiency

depends on percentage of hydroxyl radical (OH[•]) present in the reaction. In the mechanism upon UV exposure electrons get excited from VB to CB creating holes (h^+) behind as shown by Eq. (1). These electron-hole pair participate separately in the formation of hydroxyl free radical (OH[•]). On the basis of photocatalytic mechanism, Eqs. (2), (3) and (4) represents the formation of hydroxyl free radical (OH[•]) via photo-oxidation of H₂O by holes (h^+) and photo-reduction of O₂ by electron (e^-) under UV exposure, respectively. This hydroxyl free radical (OH[•]) further react with malachite green (MG) dye results in breaking of its chemical bonds and turned into harmless degraded product as shown in Eq. (5).

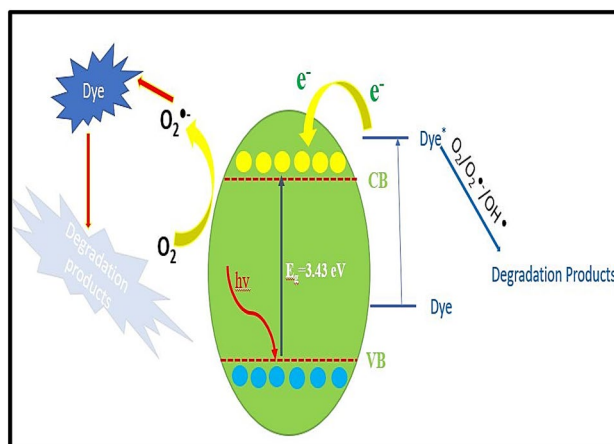
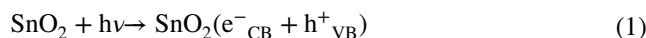


Fig. 9 Proposed Schematic mechanism for Photocatalytic degradation of malachite green dye

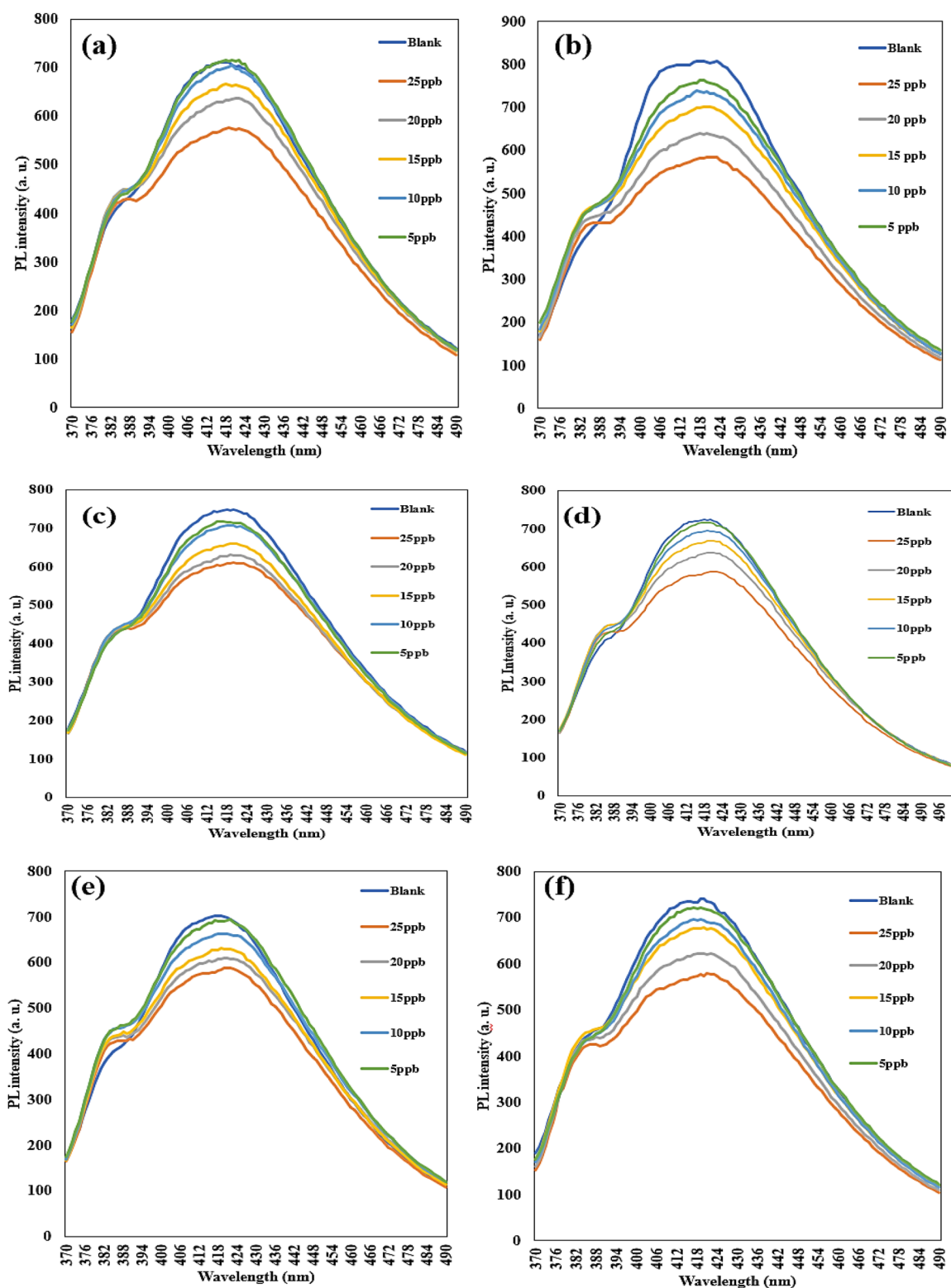


Fig. 10 PL emission spectra of the aqueous suspension of **a** pure SnO_2 ; **b** 1 mol%; **c** 3 mol%; **d** 5 mol%; **e** 7 mol% and **f** 10 mol% Sb-doped SnO_2 samples in the presence of Cd^{2+} at different concentrations; **g** calibration fitting curve of the linearity of Stern–Volmer plot

for Cd^{2+} at different concentrations in the aqueous suspension of pure SnO_2 ; **h** 1 mol%; **i** 3 mol%; **j** 5 mol%; **k** 7 mol% and **l** 10 mol% Sb-doped SnO_2 samples

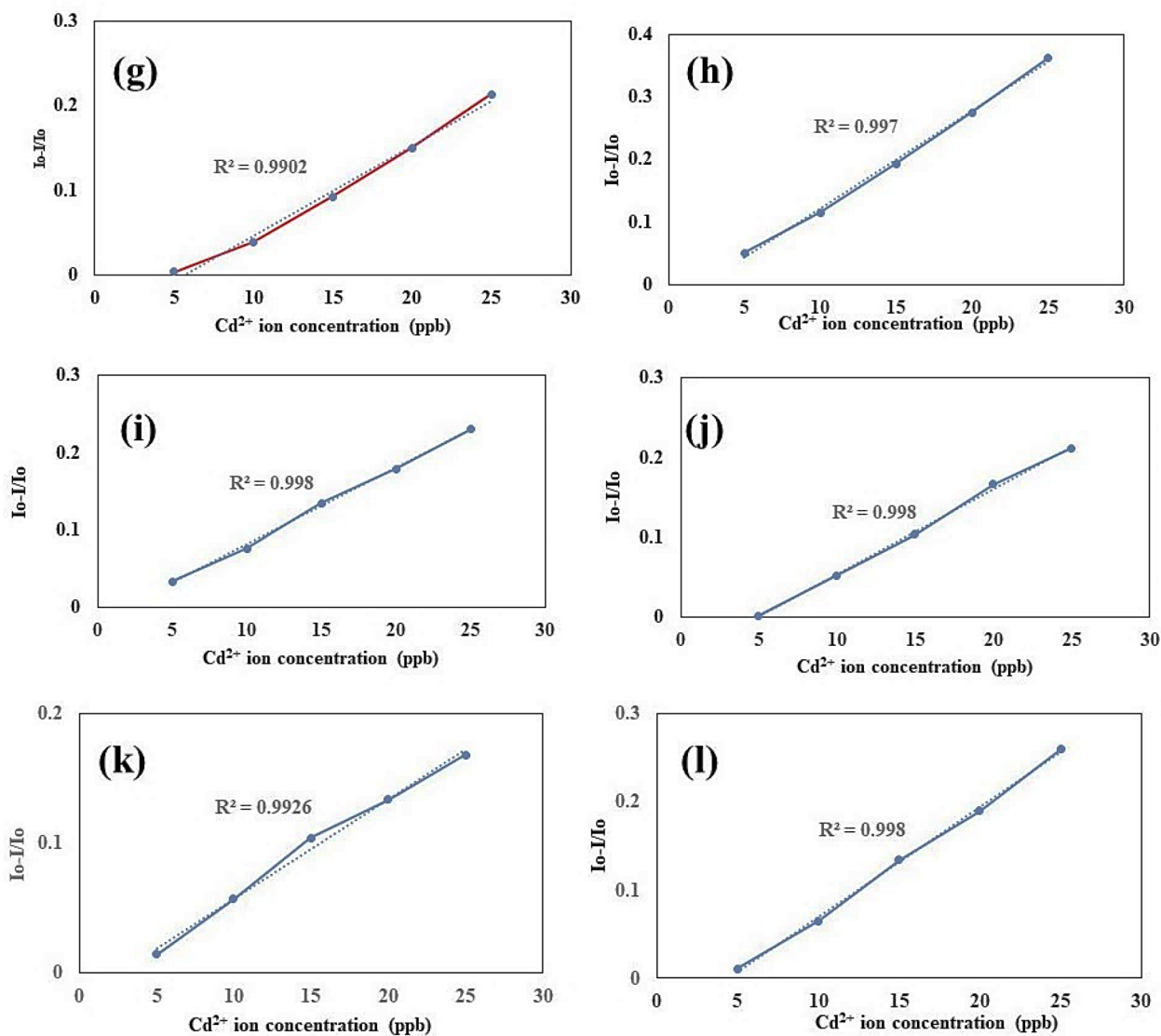
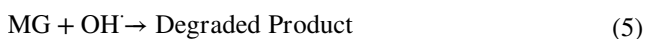


Fig. 10 (continued)



The Quenching Effect of Cd²⁺ Ion on PL of Luminescent Undoped and Sb-doped SnO₂

In the present evaluation, the optical response of pure and antimony-doped SnO₂ samples have been utilised with respect to the change in fluorescence against different Cd²⁺ ion concentrations (0, 5, 10, 15, 20 and 25 ppb) in the aqueous media.

These prepared aqueous samples of undoped and Sb-doped SnO₂ shows excellent response to Cd²⁺ ion. Figure 10a-f shows PL emission spectra of undoped and Sb-doped SnO₂ through experiments, which were performed using different concentration of Cd²⁺ as a analyte keeping excitation wavelength at

Table 2 K_{SV}, R² and LOD (ppb) values of synthesized samples

Sample	K _{SV}	R ²	LOD (ppb)
Undoped SnO ₂	0.0106	0.9902	12.1340
1% Sb-doped SnO ₂	0.0156	0.9970	3.8499
3% Sb-doped SnO ₂	0.0099	0.9980	3.2046
5% Sb-doped SnO ₂	0.0107	0.9980	3.2019
7% Sb-doped SnO ₂	0.0077	0.9926	3.1915
10% Sb-doped SnO ₂	0.0125	0.9980	3.1807

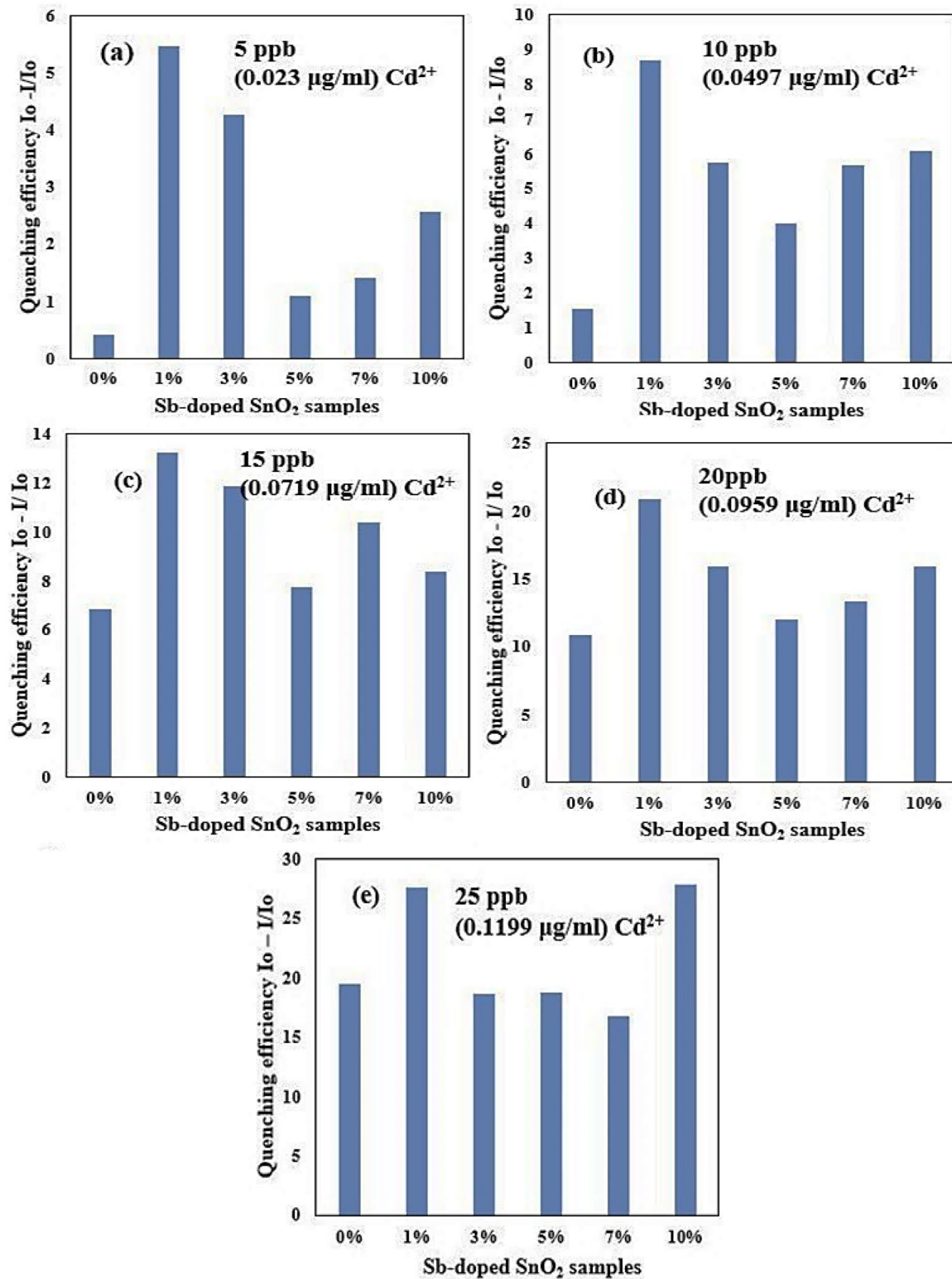


Fig. 11 Bar graphs representing fluorescence quenching efficiency obtained for Sb-doped SnO_2 solution with Cd^{2+} at **a** 5 ppb; **b** 10 ppb; **c** 15 ppb; **d** 20 ppb; **e** 25 ppb

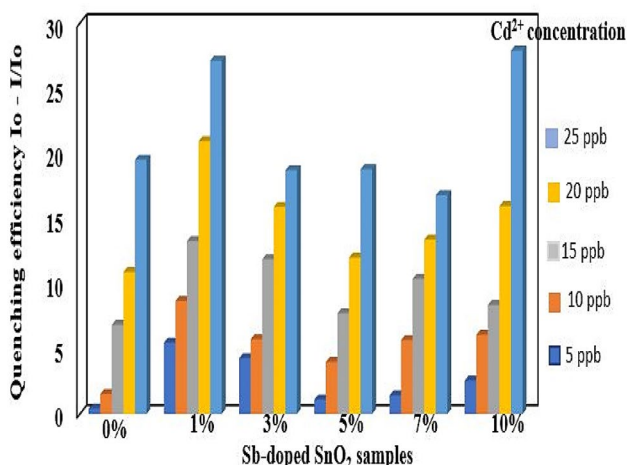


Fig. 12 Comparison of quenching efficiencies of Sb-doped SnO₂ samples at different Cd²⁺ ion concentrations

($\lambda_{\text{ex}} = 350 \text{ nm}$). From Fig. 10, it is evaluated that there occurs a quenching in fluorescence intensity with the addition of Cd²⁺ as an analyte in all samples and with increase in concentration of quencher (Cd²⁺) fluorescence intensity decrease gradually without having appreciable change in the spectral profile of all samples. Figure 10g-l represents the Stern-Volmer plot of undoped and Sb-doped SnO₂ samples, which describes the relationship between fluorescence intensity and analyte concentration. These graphs show a good linearity with regression coefficients as 0.9902, 0.9970, 0.9980, 0.9980, 0.9926 and 0.9980 for 0%, 1%, 3%, 5%, 7% and 10% Sb-doped SnO₂ samples, respectively. The Stern-Volmer plot is between $I_0 - I/I_0$ vs. analyte (Cd²⁺) concentration, where I_0 and I are fluorescence intensity before and after addition of analyte. IUPAC definition, $\text{LOD} = 3\sigma/\text{slope}$ (where σ represents standard deviation of linear curve), has been opted for the calculation of the Limit of Detection (LOD). Table 2 represents LOD, K_{SV} and R^2 values of Stern Volmer curves of all samples. All samples except pure SnO₂ shows LOD value below the current limit (10 ppb). Among all samples LOD value of Cd²⁺ for 10%

Sb-doped SnO₂ sample (3.18 ppb) is lowest. In addition to the study of quenching of fluorescence intensity another parameter, quenching efficiency has also been calculated. Quenching efficiency has been evaluated using following equation for different Cd²⁺ concentration:

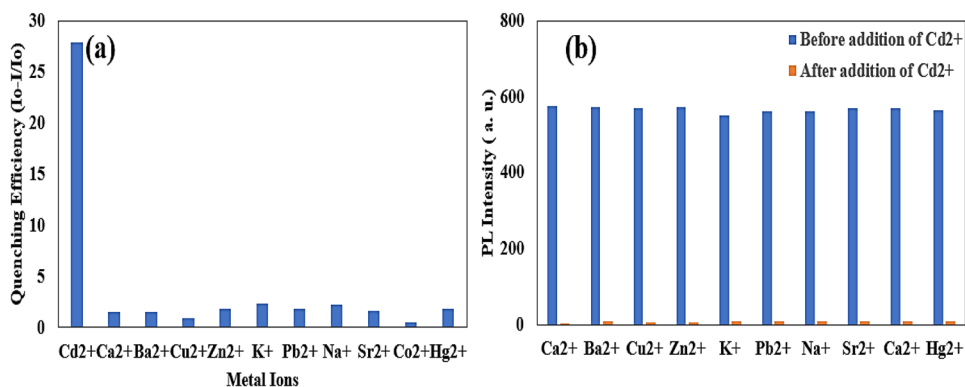
$$QE = I_0 - I/I_0$$

Figure 11a-e represents the quenching efficiency in form of bar graphs for undoped and doped samples in presence of Cd²⁺ different concentration range as (5, 10, 15, 20, 25 ppb). Among all 10% Sb-doped SnO₂ shows maximum fluorescence quenching as 0.27 as compared to other samples as seen in Fig. 12, which depicts 10%-Sb doped SnO₂ have maximum sensitivity towards Cd²⁺ analyte.

Sensing of 10% Sb-doped SnO₂ Towards Other Heavy Metal Ions and Selectivity Towards Cd²⁺

Figure 13a represents the quenching efficiencies of different heavy metal ions (Cd²⁺, Ca²⁺, Hg²⁺, Co²⁺, Sr²⁺, Na⁺, Pb²⁺, K⁺, Zn²⁺, Cu²⁺ and Ba²⁺) towards 10% Sb-doped SnO₂. From this it can be clearly seen that quenching efficiency was maximum for Cd²⁺, whereas other heavy metal ions Ca²⁺, Hg²⁺, Co²⁺, Sr²⁺, Na⁺, Pb²⁺, K⁺, Zn²⁺, Cu²⁺ and Ba²⁺ shows very minimum effect. Therefore, 10% Sb-doped SnO₂ can be utilised as a good fluorescent sensor to detect Cd²⁺ ions in drinking water. For the further sensing studies, there was a need to analyse a competing effect of heavy metal ions. So, to check the selectivity of 10% Sb-doped SnO₂ towards Cd²⁺ in the co-existence of other heavy metal ions, an experiment was performed. Here, PL intensity of 10% Sb-doped SnO₂ was recorded with and without addition of 3 mL (25 ppb) Cd²⁺ aqueous solution having 3 mL (25 ppb) aqueous solution of other heavy metal ions as shown in Fig. 13b. From this it can be clearly deduced that there occur a prominent decrease in luminescence intensity after addition of aqueous solution of Cd²⁺. Hence, it is proved that the presence of other heavy metal ions does not disturb selectivity of Cd²⁺ for 10% Sb-doped SnO₂.

Fig. 13 a Selectivity bar diagram of the fluorescence quenching of 10% Sb-doped SnO₂ (3 mL) towards Cd²⁺ and other heavy metal ions with concentration of 25 ppb. **b** Comparison of luminescence intensity before and after addition of Cd²⁺ ion in aqueous solutions of other metal ions



Conclusion

For the good yield of pure and Sb-doped SnO₂ samples, a facile and simple hydrothermal methods is utilised. Morphological, photo catalytical and sensing abilities of the synthesized samples sturdily depends upon doping concentrations. 10% Sb-doped SnO₂ has been observed to have dye degradation efficiency 80.86%, which make it efficient photocatalyst. Additionally, undoped and Sb-doped SnO₂ have been utilised for sensing of Cd²⁺ in drinking water even at ppb level through fluorescence quenching. Doping of Sb upto 10% in SnO₂ shows a highest quenching efficiency of 27% compared to other undoped and doped samples with Cd²⁺ concentration 0.11 µg/mL and limit of detection (LOD) as low as 0.0152 µg/mL. This work proves that appropriate doping in SnO₂ sample make it efficient photocatalyst for degradation of organic pollutant (dyes) in water and fluorescent sensor for the detection of heavy metal ions in drinking water even as low as ppb level. Despite the fact that numerous studies have been conducted on the modification of the SnO₂ surface to enhance its photocatalytic activity, there has been little research on the enhancement of SnO₂ particle photocatalytic activity under visible light through doping or/and surface modification. As, antimony doped SnO₂ photocatalyst have outstanding photocatalytic activity, heavy metal sensing ability, high adsorption capacity, and high stability. Further, antimony doped SnO₂ photocatalyst complete photodegraded the biologically non-biodegradable POPs. Therefore, more investigation is required to develop similar type of photocatalysts that can selectively degrade the pollutants under visible light irradiation, acting as a complement to biological techniques, because the low toxicity contaminants can be easily degraded by biological means while many of the highly hazardous materials are non-biodegradable.

Acknowledgements One of the authors, Deepika Garg is grateful to University Grants Commission (UGC), New Delhi, India, for providing senior research fellowship. Heena, one of another is also thankful to the UGC, New Delhi, India, for providing financial support under College for Potential and Excellence research grant with reference number KCP/2020/MS/2174–2179.

Author Contributions Deepika Garg: Performed the experimentation. Gurdeep Singh, Heena Rekhi, Manpreet Kaur, Rajpal Verma: Helped in performing the experiments. Karamjit Singh and Ashok Kumar Malik: Helped in writing and supervised the research work.

Funding The authors did not receive support from any organization for the submitted work and have no financial or non-financial interests to disclose.

Data Availability Data and material information is provided and will be shared on request.

Declarations

Ethics Approval There are no ethic approvals required for this research work.

Consent to Participate All authors will participate in the revision of the manuscript.

Consent for publication All authors agree for the publication.

Conflicts of Interest/Competing Interests All the authors declare that there is no conflict of interest.

References

- Rubin HN, Reynolds MM (2019) Amino-incorporated tricarboxylate metal-organic framework for the sensitive fluorescence detection of heavy metal ions with insights into the origin of photoluminescence response. *Inorg Chem* 58(16):10671–10679
- Kaur H, Bhatti HS, Singh K (2020) Pr doped SnO₂ nanostructures: morphology evolution, efficient photocatalysts and fluorescent sensors for the detection of Cd²⁺ ions in water. *J Photochem Photobiol A* 388:112144
- Zhu YF, Wang YS, Zhou B, Yu JH, Peng LL, Huang YQ, Wang XF (2017) A multifunctional fluorescent aptamer probe for highly sensitive and selective detection of cadmium (II). *Anal Bioanal Chem* 409(21):4951–4958
- Ding SB, Wang W, Qiu LG, Yuan YP, Peng FM, Jiang X, Zhu JF (2011) Surfactant-assisted synthesis of lanthanide metal-organic framework nanorods and their fluorescence sensing of nitroaromatic explosives. *Mater Lett* 65(9):1385–1387
- George G, Edwards CS, Hayes JI, Yu L, Ede SR, Wen J, Luo Z (2019) A novel reversible fluorescent probe for the highly sensitive detection of nitro and peroxide organic explosives using electrospun BaWO₄ nanofibers. *J Mater Chem C* 7(47):14949–14961
- Håkansson K, Coorey RV, Zubarev RA, Talrose VL, Håkansson P (2000) Low-mass ions observed in plasma desorption mass spectrometry of high explosives. *J Mass Spectrom* 35(3):337–346
- Akpan UG, Hameed BH (2009) Parameters affecting the photocatalytic degradation of dyes using TiO₂-based photocatalysts: a review. *J Hazard Mater* 170(2–3):520–529
- Borker P, Salker AV (2006) Photocatalytic degradation of textile azo dye over Ce_{1-x}Sn_xO₂ series. *Mater Sci Eng B* 133(1–3):55–60
- Ahmed AS, Singla ML, Tabassum S, Naqvi AH, Azam A (2011) Band gap narrowing and fluorescence properties of nickel doped SnO₂ nanoparticles. *J Lumin* 131(1):1–6
- Bouras K, Rehspringer JL, Schmerber G, Rinnert H, Colis S, Ferblantier G, Slaoui A (2014) Optical and structural properties of Nd doped SnO₂ powder fabricated by the sol-gel method. *J Mater Chem C* 2(39):8235–8243
- Kolesnikov IE, Kolokolov DS, Kurochkin MA, Voznesenskiy MA, Osmolovskiy MG, Lähderanta E, Osmolovskaya OM (2020) Morphology and doping concentration effect on the luminescence properties of SnO₂: Eu³⁺ nanoparticles. *J Alloys Compd* 822:153640
- Bak T, Nowotny J, Rekas M, Sorrell CC (2002) Photo-electrochemical hydrogen generation from water using solar energy. Materials-related aspects. *Int J Hydrog Energy* 27(10):991–1022
- Kamat PV (2002) Photoinduced transformations in semiconductor-metal nanocomposite assemblies. *Pure Appl Chem* 74(9):1693–1706

14. Huang Y, Li G, Feng J, Zhang Q (2010) Investigation on structural, electrical and optical properties of tungsten-doped tin oxide thin films. *Thin Solid Films* 518(8):1892–1896
15. Batzill M, Diebold U (2005) The surface and materials science of tin oxide. *Prog Surf Sci* 79(2–4):47–154
16. Senthilkumar V, Senthil K, Vickraman P (2012) Microstructural, electrical and optical properties of indium tin oxide (ITO) nanoparticles synthesized by co-precipitation method. *Mater Res Bull* 47(4):1051–1056
17. Banyamin ZY, Kelly PJ, West G, Boardman J (2014) Electrical and optical properties of fluorine doped tin oxide thin films prepared by magnetron sputtering. *Coatings* 4(4):732–746
18. Obaida M, Moussa I, Boshta M (2015) Low sheet Resistance FDoped SnO₂ Thin Films deposited by novel spray pyrolysis technique. *Int J ChemTech Res* 8:239–247
19. Giraldi TR, Escote MT, Maciel AP, Longo E, Leite ER, Varela JA (2006) Transport and sensors properties of nanostructured antimony-doped tin oxide films. *Thin Solid Films* 515(4):2678–2685
20. Senguttuvan TD, Malhotra LK (1996) Sol gel deposition of pure and antimony doped tin dioxide thin films by non alkoxide precursors. *Thin Solid Films* 289(1–2):22–28
21. Jain G, Kumar R (2004) Electrical and optical properties of tin oxide and antimony doped tin oxide films. *Opt Mater* 26(1):27–31
22. Babar AR, Shinde SS, Moholkar AV, Bhosale CH, Kim JH, Rajpure KY (2011) Physical properties of sprayed antimony doped tin oxide thin films: the role of thickness. *J Semicond* 32(5):053001
23. Bhat JS, Maddani KI, Karguppikar AM (2006) Influence of Zn doping on electrical and optical properties of multilayered tin oxide thin films. *Bull Mater Sci* 29(3):331–337
24. Vijayalakshmi S, Venkataraj S, Subramanian M, Jayavel R (2008) Physical properties of zinc doped tin oxide films prepared by spray pyrolysis technique. *J Phys D* 41(3):035505
25. Al-Hamdi AM, Sillanpää M, Bora T, Dutta J (2016) Efficient photocatalytic degradation of phenol in aqueous solution by SnO₂:Sb nanoparticles. *Appl Surf Sci* 370:229–236
26. Tayade RJ, Natarajan TS, Bajaj HC (2009) Photocatalytic degradation of methylene blue dye using ultraviolet light emitting diodes. *Ind Eng Chem Res* 48(23):10262–10267
27. Ahmed MA, El-Katori EE, Gharni ZH (2013) Photocatalytic degradation of methylene blue dye using Fe₂O₃/TiO₂ nanoparticles prepared by sol–gel method. *J Alloys Compd* 553:19–29
28. Sujatha K, Seethalakshmi T, Sudha AP, Shanmugasundaram OL (2020) Photoluminescence properties of pure, Fe-doped and surfactant-assisted Fe-doped tin-oxide nanoparticles. *Bull Mater Sci* 43(1):1–10
29. Qu X, Wang MH, Chen Y, Sun WJ, Yang R, Zhang HP (2017) Facile synthesis of hierarchical SnO₂ twig-like microstructures and their applications in humidity sensors. *Mater Lett* 186:182–185
30. Ansari SG, Borojerdian P, Sainkar SR, Karekar RN, Aiyer RC, Kulkarni SK (1997) Grain size effects on H₂ gas sensitivity of thick film resistor using SnO₂ nanoparticles. *Thin Solid Films* 295(1–2):271–276
31. Singh G, Kohli N, Singh RC (2017) Preparation and characterization of Eu-doped SnO₂ nanostructures for hydrogen gas sensing. *J Mater Sci Mater Electron* 28:2257–2266
32. Chen W, Zhou Q, Wan F, Gao T (2012) Gas sensing properties and mechanism of nano-SnO₂-based sensor for hydrogen and carbon monoxide. *J Nanomater* 2012:1–1
33. Weber IT, Valentini A, Probst LFD, Longo E, Leite ER (2004) Influence of noble metals on the structural and catalytic properties of Ce-doped SnO₂ systems. *Sens Actuators B* 97(1):31–38
34. Vegard L (1921) Die konstitution der mischkristalle und die raumfüllung der atome. *Z Physik* 5(1):17–26
35. Pearson GL, Bardeen J (1949) Electrical properties of pure silicon and silicon alloys containing boron and phosphorus. *Phys Rev* 75(5):865

Publisher's Note Springer Nature remains neutral with regard to jurisdictional claims in published maps and institutional affiliations.

Springer Nature or its licensor (e.g. a society or other partner) holds exclusive rights to this article under a publishing agreement with the author(s) or other rightsholder(s); author self-archiving of the accepted manuscript version of this article is solely governed by the terms of such publishing agreement and applicable law.